

Ground Feature Oriented Path Planning for Unmanned Aerial Vehicle Mapping

Chun Liu , Shuhang Zhang , and Akram Akbar

Abstract—Unmanned aerial vehicles (UAVs) are being used to take roles that were previously performed by traditional manned aircraft, such as remote sensing and photogrammetry. The standard path planning for UAV mapping is mainly executed by adopting the “lawnmower” mode. However, some situations that have sparse or repetitive features are problematic to map with this technique, given that orthoimage stitching relies heavily on the number and quality of image tie points. Traditional path planning can result in some unregistered images due to a lack of tie points. This paper proposes a ground feature oriented path-planning method for UAV mapping. The method first estimates the distribution of the ground feature points from a lower-resolution image. Then, image footprints are selected by applying a three-step optimization. The flight path for the UAV is then generated by solving the “grouped traveling salesman” problem. This approach ensures the georegistration of images during orthoimage stitching while maximizing the orthoimage coverage. Two cases, including a simulation and a real-world case, together with standard path-planning modes with different overlaps, are selected to evaluate the proposed method. The results show that the proposed method covers the same area with the smallest number of images. The model excludes problematic areas from the scanning path to generate a more efficient processing dataset.

Index Terms—Path planning, Scale-invariant feature transform (SIFT), submodular optimization, unmanned aerial vehicle (UAV).

I. INTRODUCTION

UNMANNED aerial vehicles (UAVs) offer the advantages of low cost, high mobility, and maneuverability. With the rapid development of UAVs and sensors, UAVs are being used to take on the roles that were traditionally played by conventional manned aircraft, notably as remote-sensing platforms. They have brought much greater levels of efficiency to many industries, such as powerline inspection, precision agriculture, and forest inventory management [1]–[4].

Among these industrial applications, mapping is one of the most important since accurate geoinformation provides a datum and framework for many different applications. Furthermore, mapping is an application that can take full advantage of the mobility and maneuverability of UAVs. Terrain and objects

Manuscript received October 26, 2018; revised December 12, 2018; accepted February 10, 2019. Date of publication March 8, 2019; date of current version April 17, 2019. This work was supported in part by the National Natural Science Foundation of China under Grant 41771481 and in part by the China Scholarship Council. (Corresponding author: Shuhang Zhang.)

The authors are with the College of Surveying and Geo-informatics, Tongji University, Shanghai 200092, China (e-mail: liuchun@tongji.edu.cn; shuhangz@outlook.com; 12akram@tongji.edu.cn).

Color versions of one or more of the figures in this paper are available online at <http://ieeexplore.ieee.org>.

Digital Object Identifier 10.1109/JSTARS.2019.2899369

can be 3-D reconstructed with high accuracy by processing a series of overlapped UAV images. The reconstructed 3-D models can be used to digitalize building information modeling [5], cultural heritage documentation [6], and terrain-change detection [7]. Photogrammetry [8] and structure from motion (SfM) [9] are effective techniques for reconstructing scenes from images. However, some areas are problematic to map with these techniques. Image matching is a critical step for both photogrammetry and SfM, but it relies heavily on the number and quality of image tie points. These areas have sparse or repetitive texture features, resulting in an irregular distribution of image tie points. This makes it impossible to georegister some of the captured images due to a lack of tie points. Such areas may be bare land, desert, and snow. Apart from this, water surface may provide false tie points owing to the excessive movement and reflection. Therefore, the mapping of these problematic areas using UAVs is a challenge.

There are two strategies to address the challenge: Direct georeferencing (DG) and path planning. DG relates directly to the data captured by a remote sensing system, by accurately measuring the geographic position and orientation of the sensor [10], [11]. In other words, a DG system provides the exterior orientation elements of each UAV image; so these elements need not be calculated by aerial triangulation (AT), which relies on image tie points. DG provides high-quality results, and offers excellent benefits in terms of time and cost reduction [12]. A state-of-the-art DG system for UAVs can yield a spatial object accuracy of 4.1 cm without any ground control point [13]. Nevertheless, a DG system requires overall system calibration, while the correct calibration of the sensor system cannot be guaranteed *a priori* [14]. In addition, a DG system is more expensive than an ordinary photogrammetric system. The use of path planning to address this challenge places fewer demands on the UAV platform. However, instead of the standard “lawnmower” mode, a new flight path mode has to be adopted, given that in problematic areas, it is difficult for standard path-planning methods to avoid capturing images that cannot be georegistered. Therefore, the present study set out to produce a path-planning method for ordinary surveying of UAVs to map problematic areas as completely as possible, i.e., by trying to avoid the capturing of images that cannot be registered.

Tie points are essential to image mosaicking and AT. During the process of photogrammetry and SfM, an adequate number of appropriate tie points have to be found to calculate the position and orientation of each image. Common image-matching methods are based on radiometric information. Within

photogrammetry and SfM procedures, a scale-invariant feature transform (SIFT) [15] detector, together with random sample consensus (RANSAC) [16] is commonly used to extract and match tie points. This method and its extensions are widely used by state-of-the-art open-source photogrammetric or SfM frameworks, such as GRAPHOS [17], COLMAP [18], Mic-Mac [19], and VisualSfM [20]. Commercial software, including *Pix4Dmapper*, *ContextCapture*, and *PhotoScan*, also rely on a similar type of feature extraction. These extractors are effective when dealing with feature-rich images [21], but may return poor results when dealing with a sparse or repetitive texture. Image matching for problematic areas often takes advantage of special algorithms, such as PCA-SIFT [22], line descriptors [23]–[25], and graph-based tie point matching [26], [27]. Some methods barely optimize the SIFT parameters, such that it is possible to increase the accuracy of image matching between images of different resolutions [28]–[30]. These methods enhance the robustness of image matching, although they may fail to deal with images with “no features” at the scale of aerial mapping (e.g., images of snow). Therefore, the proposed study seeks to produce a flight path for UAV mapping that would not capture problematic images for feature detection or images that may contain false tie points.

General research into path planning for UAV mapping has mainly focused on dealing with obstacles or complex-shaped target areas [31], [32]. This is a subset of coverage path planning (CPP), which determines the path that passes over all points in an area of interest, while avoiding obstacles [33]. Multiple path-planning methods were studied as a means of generating an optimal flight path with different targets, including the minimum number of turns [34]–[36], the completion time [37], [38], and energy consumption [39], [40]. On the other hand, CPP can be abstracted using model-based view planning, which assumes some prior knowledge about the scene [41]. Model-based view planning was proven to be NP-complete [42], but reaching the global optimal can be rather difficult. Therefore, solving is generally divided into two steps: 1) selection of a set of viewpoints to fully cover the target area and 2) calculation of a path connecting every viewpoint. To date, some studies have addressed view planning that would enable a UAV to capture the data for a 3-D scene. Martin *et al.* proposed a view-planning framework for 3-D reconstruction applications using UAVs [41]. Genetic algorithms were used to optimize image locations in terms of coverage and accuracy. Jing and Shimada presented a two-step method for finding near-optimal views that would allow UAVs to cover the surfaces of 3-D targets [43]. In particular, photogrammetric network design is also related to view planning. The goal of photogrammetric network design is to capture a complete and precise point cloud under the constraints of photogrammetric 3-D reconstruction. This has been implemented in the field of cultural heritage documentation and has reached a high average accuracy of 10 mm [44]. Ahmadabadian *et al.* presented an automated network design for close-range photogrammetry that was capable of micron-level accuracy [45]. These methods involve a rigorous design of the network, but incur high algorithmic complexity and demand careful implementation. This study addresses the two-step view-planning problem. However,

rather than the rigorous network design, we concentrate on the image coverage for the problematic area.

In recent years, new methods of information-driven path planning for outdoor aerial 3-D reconstruction have been developed [46]–[49]. The views were planned based on the information acquired from the camera. The amount of information in an image is determined by the coverage of the target. Popovi *et al.* introduced an informative path-planning framework for active weed classification using UAVs. They generated adaptive plans according to information-theoretic objectives, enabling the UAV to gather data efficiently [46]. From the viewpoint of 3-D data capture, Palazzolo and Stachniss proposed an online approach to select the next best view that maximizes the expected information gain of new measurements [47]. The study by [48] and [49] was similar in which they both produced a model-based view-planning method to maximize the information gain. The 3-D scene was voxelized and the information of an image was related to the number of voxels in view. They then leveraged the submodularity of the object function and used a greedy algorithm to approximate the otherwise intractable optimization problem [50]. This study was also information driven, but with a different objective. The information used in this study was related to the ground feature and the objective was a complete coverage of the problematic area.

In summary, the present study addresses the problem of path planning to allow ordinary surveying of UAVs to map problematic areas as completely as possible. The technical contributions are as follows.

- 1) Estimation of feature point distribution for path planning based on a low-resolution aerial/satellite image.
- 2) Produce an image footprint (i.e., camera position and orientation) generation method that guarantees image georegistration and maximum 3° overlap coverage.

II. GROUND FEATURE ORIENTED PATH PLANNING

In this section, we discuss the path-planning methodology used to acquire as complete an ortho image as possible of problematic areas. For the complexity reduction, this method is based on the hypothesis that the ground is flat and there is no terrain fluctuation in the target area. The proposed methodology follows the steps of model-based view planning and consists of four main parts—ground feature point estimation, candidate footprint set initialization, optimal footprint set selection, and waypoint generation—as illustrated in Fig. 1.

The first difficulty to overcome is the leveraging of prior knowledge of the target area. In other words, the locations of potential tie points must be estimated. Therefore, we used a modified detector and support vector machine (SVM) filter to detect feature points from a low-resolution image of the target area. The next step is candidate footprint initialization. The footprints were initialized considering the camera specifications and required ground sample distance (GSD). The information for each footprint was then calculated, while any footprint that could not be georegistered was removed from the candidate footprint set. Subsequently, three-step optimization was used to select the optimal footprint set, which contains ground feature point

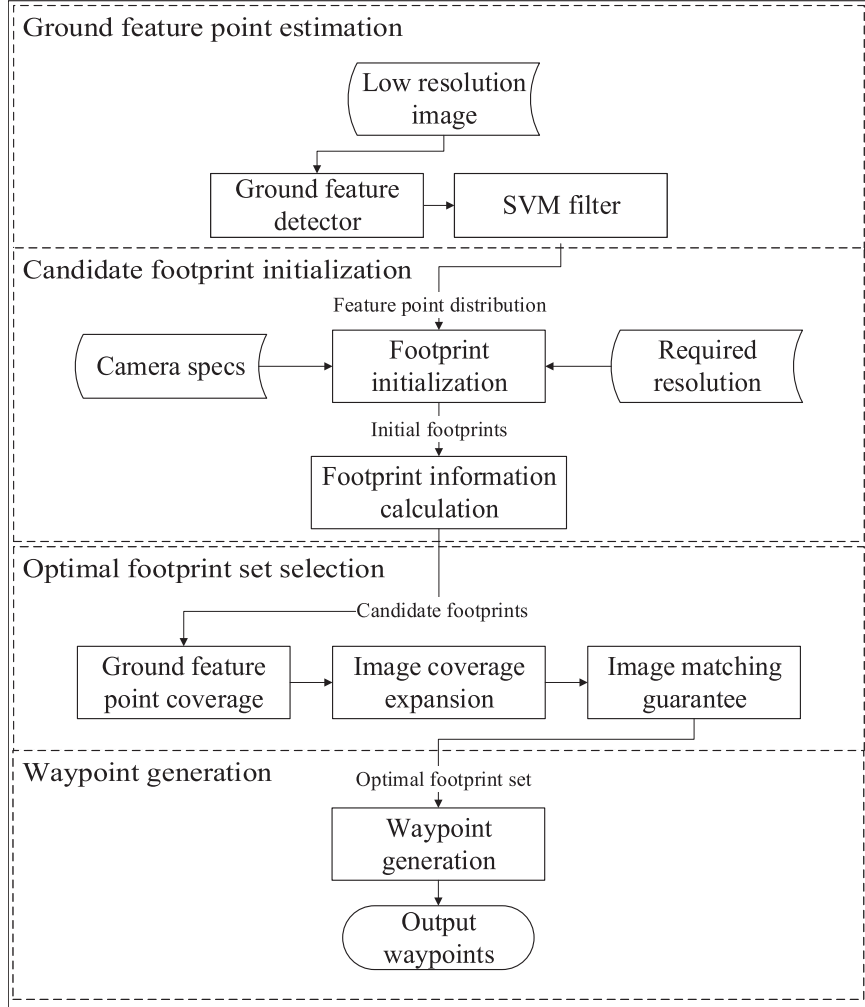


Fig. 1. Methodology overview.

coverage, image coverage expansion, and an image-matching guarantee. The selected optimal footprint set maximizes the image coverage of the target area, while ensuring the mosaicking of the ortho image. The final step is to connect the footprints to generate waypoints for the UAV from the optimal footprint set.

A. Ground Feature Point Estimation

To conduct ground feature oriented path planning, the distribution of the ground features should be estimated first. The *ground feature* described in this paper refers to the texture feature of the ground. Tie points for image matching will be extracted from the texture. Since tie points form the basis of AT, estimating them well will enable the design of an appropriate flight path. The input of the proposed method is an existing satellite or aerial image of the target area. The GSD of the image should be within an acceptable range, depending on the required surveying GSD. The ground feature information is lost as the GSD decreases, and it is not possible to estimate the ground features for path planning when using a very coarse image. The acceptable GSD range is discussed in Section II-A1. Another

factor to be considered within the estimation is the environmental impact, which is discussed in Section II-A2.

1) *Ground Feature Point Detection*: Central to the proposed ground feature point detection method is SIFT [15], in the same way as the majority of photogrammetry and SfM pipelines that use it or its extensions as a feature extractor. Since our goal is to estimate the distribution of feature points on the ground, we adopted a similar method. The principal of SIFT detection is the detection of the local extremes in the differences in the Gaussian (DoG) D , which is the difference between two Gaussian images L in the scale space

$$D(x, y, \sigma(o, s)) = L(x, y, \sigma(o, s + 1)) - L(x, y, \sigma(o, s)) \quad (1)$$

$$\text{where } \sigma(o, s) = \sigma_0 2^{o + \frac{s}{8}}$$

$$o \in [0, \dots, O - 1], s \in [0, \dots, S + 2]. \quad (2)$$

o is the octave index, while s is the scale index; O and S are the number of octaves and scales. The SIFT keypoints are then extracted from the DoG pyramid, compared to their 26 neighboring pixels from levels s , $s + 1$ and $s - 1$ [15].

TABLE I
SIFT PARAMETERS TO BE TUNED

Parameter name	Description	Adjustment
Sigma	The sigma value for initial Gaussian smoothing.	Reduce
Octaves	The number of octaves.	Reduce
Scales	The number of scales sampled in each octave.	Increase
Edge threshold	The maximum threshold for feature ratio of principle curvatures.	Reduce
Contrast threshold	The minimum threshold on feature contrast.	Reduce

To achieve the proposed SIFT-based ground feature point detection method, the GSD of the input image G_p should be within a certain range, relative to the surveying GSD G_s , given that the number of octaves O is limited in the photogrammetry and SfM pipeline. This range is related to the building of the scale space of the SIFT. In the scale space, the input image is down sampled by a factor of 2 for every octave. Therefore, the factor of the image in the top octave will be 2^{O-1} . On the other hand, the images in each octave are Gaussian blurred with the sigma in (2). The maximum sigma in the scale space σ_m will be $\sigma_0 2^{O+\frac{2}{S}}$ [15]. The smoothing with σ_m results in a loss of image detail. Details smaller than $\sqrt{\sigma_m}$ are essentially removed [51], such that the smoothing is equivalent to down sampling with the factor $\sqrt{\sigma_m}$. To ensure that the input image contains a feature that can be detected in images captured by UAV, G_p and G_s should have the following relation:

$$G_p \leq 2^{O-1} \sqrt{\sigma_m} G_s. \quad (3)$$

To the best of our knowledge, the most commonly used values for σ_0 , O , and S in photogrammetry, and SfM pipelines are 1.6, 4, and 3 [17]–[19]. By substituting these values into (3), we can approximate G_p to be no more than $50G_s$.

After an image is input, we modify the SIFT detector to estimate the ground feature points. The ultimate goal of this estimation is to eliminate false positives; so in this step, the SIFT parameters are tuned to detect more features within the low-GSD input image. There are 17 main intrinsic parameters that control the response of the SIFT, some of which are robust, while others are relatively sensitive [28]. The parameters we tune are listed in Table I.

These parameters are sensitive to tuning. As such, we tuned them to make SIFT more adaptive to a low-GSD image. The *sigma* value defines the level of the initial Gaussian smoothing of each octave, which has a significant effect on the number of feature points. Reducing *sigma* can yield a greater number of points because the contribution of the neighborhood to the pixel value in the smoothed image is smaller. Furthermore, a low-GSD image can be regarded as being a Gaussian-blurred high-GSD image. Reducing the *octaves* results in fewer octave levels and smaller down-sampled factors. Feature points of the high octave levels of the input image are not needed since the

features of such high levels cannot be detected from a single UAV image during the reconstruction process. Increasing the value of *scales* can lead to the detection of more feature points from a low-GSD image. The *edge threshold* is used to filter edge-like features. The edges become shorter as the image GSD decreases, so the *edge threshold* should also be decreased to preserve the features. The *contrast threshold* is used to filter out weak features in low-contrast regions. Increasing it can also preserve the features in low-GSD images. However, optimizing the values of these parameters is beyond the scope of this study. We use a set of empirical values in the case study. Readers may refer to [28]–[30] for details on the optimization of SIFT parameters.

2) *Feature Point Filtering*: The goal of ground feature point estimation for path planning is eliminating false positives. In practice, however, some areas may not provide reliable tie points for image matching, although they have rich textures that can provide several feature points. These areas often consist of vegetation that may sway in the wind and water with waves that reflect the sunlight. This phenomenon makes it difficult to locate proper tie points between images that include these objects. Considering this, feature points located in unreliable areas should be filtered. For each detected feature point vector \mathbf{p}_i in the SIFT point set P_f generated in the previous step, a classifier should output the class label $y_i \in \{-1, 1\}$ to indicate whether a feature point has been filtered. Since the dimension is relatively large, an SVM [52] satisfies this requirement. During the training phase, the 128-dimension SIFT descriptor, together with the RGB information of the feature point, forms the vector \mathbf{p}_i with dimension $d = 131$. The SVM tries to build a $d - 1$ dimensional hyperplane to separate these vectors into two classes (tie points $\mathbf{p}_{i,1}$ and others $\mathbf{p}_{i,-1}$) with a maximal margin. The target of SVM training is to solve the following optimization problem:

$$\begin{aligned} \min_{w, b, \xi} & \frac{1}{2} \mathbf{w}^T \mathbf{w} + D \sum_{i=1}^N \xi_i \\ \text{subject to} & \\ y_i (\mathbf{w}^T \phi(\mathbf{p}_i) + b) & \geq 1 - \xi_i \\ \xi_i & \geq 0, C \geq 0, i = 1, 2, \dots, N \end{aligned} \quad (4)$$

where ξ_i measures the degree of misclassification, D is the penalty parameter of the classification errors, \mathbf{w} is the support vector, and b is the offset of the hyperplane. $\phi(\mathbf{p}_i)$ is the kernel function that maps the data into the feature space. The kernel function can be a linear, polynomial, sigmoid, or radial basis function, which is selected during our training session after comparison. The training data are derived from the 3-D tie points generated from actual UAV images. The data contain the scenarios of water, vegetation, bare land, and other man-made objects. The optimization problem of (4) can be solved by quadratic programming. After the training session, the classifier can label the feature point vector \mathbf{p}_i with y_i , which indicates whether the feature point is a tie point. Ultimately, these feature points labeled as tie points $\mathbf{p}_{i,1}$ are preserved.

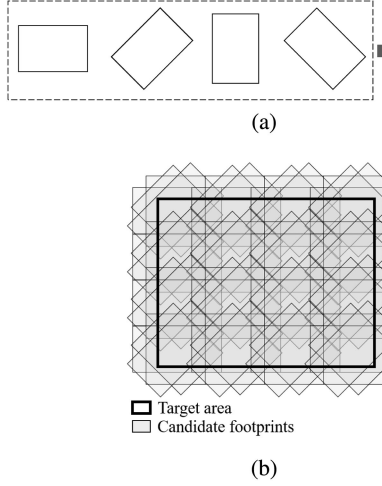


Fig. 2. Candidate footprint initialization. (a) Initialize candidate footprints with different orientations. (b) Candidate footprints densely cover target area.

B. Candidate Footprint Initialization

The goal of this optimization task is to select an optimal subset of the image footprints, such that a candidate footprint set C should be initialized first. The set C should better contain all possible image footprints, so we create dense initial footprints with multiple orientations, as shown in Fig. 2. We assume that the altitude of each footprint is the same, as determined by the surveying GSD. The size of each footprint is, therefore, calculated using the camera model and the flight altitude. The initial footprint set consists of units with four orientations (0° , 45° , 90° , and 135°), considering the computational cost and UAV execution [see Fig. 2(a)]. Each unit is then sampled within the target area with a high overlap [see Fig. 2(b)]. The set C is constructed for the next step of selection. The variety of initial footprints $c_i \in C$ can provide a better optimization result at an acceptable cost.

C. Optimal Footprint Set Selection

The goal of this method is to find an optimal footprint set that maximizes the image coverage, while all footprints can be georegistered. Therefore, this step involves optimizing the footprint set with the input of the tie points $p_{i,1}$ and the initial footprint set C . Each tie point p has a location (x, y) , while each footprint c has a location and orientation (x, y, θ) , $\theta \in [0^\circ, 360^\circ]$. We built a three-step optimization framework for the footprint set selection, with the aid of submodular optimization [50].

1) *Problem Definition:* Let $\text{FP} = \{\text{fp}_1, \text{fp}_2, \dots, \text{fp}_n\} \subset C$ be the selected footprint set, where $|\text{FP}|$ denotes the footprint count. The optimization problem to be solved is

$$\begin{aligned} \text{FP}^* = \arg \min_{\text{FP} \subset \mathcal{P}(C)} |\text{FP}| \\ \text{s.t. } f(\text{FP}) \geq q \end{aligned} \quad (5)$$

where $\mathcal{P}(C)$ is the power set of the initial footprint set C and $f(\text{FP})$ is the constraint function that is greater or equal to a given

Input: Candidate footprint set C

Output: A subset $\text{FP}^* \subset C$ that collects all information with an approximate minimum count.

```

1: function GREEDY( $C$ )
2:    $IG_{list} \leftarrow \forall fp \in C \text{ calculate } IG(fp, \phi)$ 
3:    $IG_{list} \leftarrow IG_{list} \setminus fp \text{ where } IG(fp, \phi) < q_0$ 
4:    $FP^* \leftarrow \phi$ 
5:    $fp_0 \leftarrow \max(IG_{list})$ 
6:   while  $IG(\phi, \{fp_0\}) > 0$  do
7:      $fp_0 \leftarrow \max(IG_{list})$ 
8:     Re-evaluate  $IG(fp_0, FP^*)$ 
9:     if  $IG(fp_0, FP^*) = \max(IG_{list})$  then
10:        $FP^* \leftarrow FP^* \cup fp_0$ 
11:     else
12:       Re-sort  $IG_{list}$ 
13:     end if
14:   end while
15:   return  $FP^*$ 
16: end function

```

Fig. 3. Greedy algorithm for selecting optimal footprint set.

amount q . The function

$$f(\text{FP}) = \sum_{i=1}^n I(\text{fp}_i) \quad (6)$$

where $I(\text{fp}_i)$ is the *information* that a footprint contains. The information gain $IG(fp, \text{FP})$ of a single footprint fp can be defined as

$$IG(fp, \text{FP}) = f(\text{FP} \cup \{fp\}) - f(\text{FP}). \quad (7)$$

Considering the aerial imaging process, the individual footprints are independent, while adding a single footprint never reduces the amount of information collected by the other footprints, so that (7) is positive. Therefore, (6) is monotone and submodular even though the problem (5) is NP-hard. It can be solved with a greedy algorithm with a guarantee of at least a 0.63 approximation ratio, relative to the optimal set [50]. The greedy algorithm is listed in Fig. 3, which is the basis for the three-step footprint set selection. The *information* $I(\text{fp}_i)$ and q_0 varies in each step.

2) *Three-Step Selection of Optimal Footprint Set:* The SfM or photogrammetry requires full coverage of the target area, image georegistration, and sufficient overlap. Therefore, the footprint selection must fulfill these requirements. A three-step optimization is implemented, which contains 1) *footprint coverage of ground feature points*, 2) *image coverage expansion*, and 3) *image matching guarantee*. All these steps are submodular and can be optimized by the algorithm described in Fig. 3. A simulated scenario (see Fig. 4), which is also the case in Section III-A, is used to illustrate each step of the proposed method.

The objective of step 1 is to select a minimum number of footprints to cover all ground feature points. Therefore, we define the *information* here as the number of tie points that a footprint

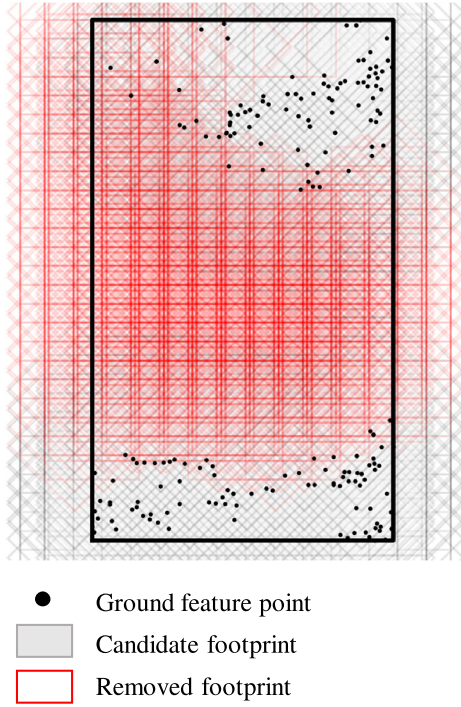


Fig. 4. Simulated scenario. Footprints whose information is less than q_0 are removed (marked in red).

covers

$$I_1(\text{fp}_i) = \sum_{p \in \text{fp}_i} p. \quad (8)$$

The q_0 in line 3 of Fig. 3 is the threshold for image georegistration, such that footprints with fewer than q_0 tie points will be removed. In theory, solving for the exterior orientation elements of an image pair requires at least five point correspondences. To overcome some uncertainties, q_0 is set to 10. After the implementation of the greedy algorithm in Fig. 3, a footprint set FP_1^* is generated to cover all ground feature points. The blue footprints in the left column of Fig. 5(a) correspond to FP_1^* .

The aim of the *image coverage expansion* step is to expand the image coverage of the target area while ensuring the image georegistration. Since any footprint without enough tie points is removed in the previous step, the process of line 3 of Fig. 3 is skipped. The *information* of this step is defined as being the area formed by the intersection between the footprint and uncovered surveying area A

$$I_2(\text{fp}_i) = S(\text{fp}_i \cap (A - \text{FP}_1^*)) \quad (9)$$

where function S calculates the area. This step returns a footprint set FP_2^* that makes the image coverage as large as possible. In the middle column of Fig. 5(a), red footprints are added to expand the image coverage.

Considering the 3-D reconstruction constraint, which requires that each ground point be observed at least three times, the last step *image matching guarantee* is to select extra footprints to guarantee 3° overlap of the coverage area. The *information* is

now defined as

$$I_3(\text{fp}_i) = w_1 S(\text{fp}_i \cap A_1) + w_2 S(\text{fp}_i \cap A_2) \quad (10)$$

where A_1 and A_2 are the polygons of the 1° and 2° overlaps and w_1 and w_2 are the weights, which are set to 2 and 1 from experience. The last step returns FP_3^* to guarantee image matching for the entire surveying area. A comparison of the image overlap before and after this step is shown in Fig. 5(b).

FP_3^* is shown in the green footprints of the right-hand column of Fig. 5(a). The three-step optimization outputs the optimal footprint set

$$\text{FP}^* = \bigcup_{i=1}^3 \text{FP}_i^*. \quad (11)$$

3) *Waypoint Generation With UAV Flying Constraint*: Once the optimal footprint set FP^* has been selected, the flight path of UAV can be generated by connecting the footprints in sequence. We assume that the UAV has to hover to change its orientation and that the footprints have different orientations. Given the flying constraints, footprints should be grouped by their orientations, such that the flight path (footprint sequence) can be generated using a grouped traveling salesman problem (TSP), as shown in Fig. 6. This algorithm calculates the shortest path connecting the footprints in each group (line 2 to line 7) and the shortest transition path between groups (line 7 to line 13). A waypoint list $\text{WP} = \{S, T\}$ can represent the flight path, where S denotes the permutation of footprint group FP_{θ_i} and T is the execution direction $t_i \in \{-1, 1\}$ (reverse or forward). FP_{θ_i} represents the group in which the footprints have the same orientation θ_i . In Fig. 6, $\mathbb{P}(S)$ is the full permutation of S . $\text{tsp}(\text{FP})$ of line 5 represents the solution of the TSP for the footprint set FP_{θ_i} and $\text{tsp}(S, t)$ of line 9 is the solution of the TSP for the permutation S and execution direction t . Since the number of orientation groups is relatively small, we use a traversal method to select the optimal permutation of the footprint group and their execution direction. The actual mission commands for UAVs can be generated according to WP , which determines the location and orientation of each image shutter point.

III. CASE STUDY

In this section, two experiments are discussed to evaluate the proposed ground feature oriented path-planning method, both qualitatively and quantitatively, in image registration and coverage. The method was evaluated by comparing the orthoimage stitching result from *Pix4Dmapper* with the standard “lawnmower” path-planning mode. The comparison was based on the time required for stitching, the image coverage, the 3° overlap coverage, and the mean reprojection error. The image coverage is the ratio of the target area covered by the orthoimage and the 3° overlap coverage is the ratio of the target area covered by at least three images.

The platform used for image stitching was a workstation with an Intel Core i7 6700HQ CPU, 16 GB of RAM, and a GTX 960M graphic card. The settings for reconstruction of each case were set to a predefined “3-D map” mode. First, the result was assessed in a simulated scene built using a professional rendering

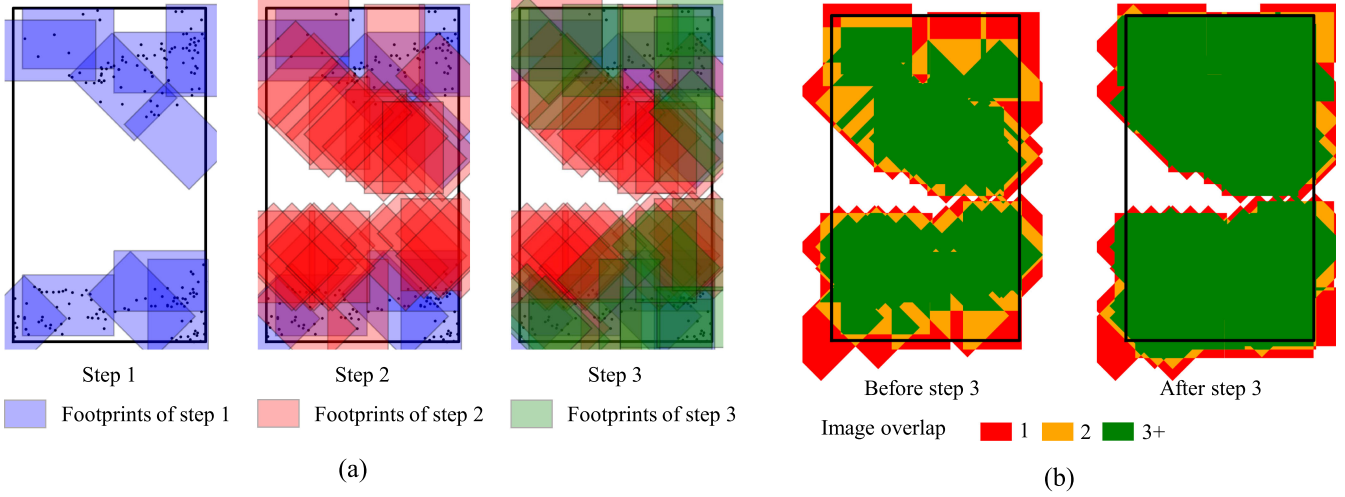


Fig. 5. Three-step selection of the optimal footprint set and overlap analysis. (a) Selection of the optimal footprint set. (b) Image overlap before and after step 3.

Input: Footprint set FP^* with different orientations θ_i .

Output: A waypoint list $WP = \{S, T\}$ that visits every footprint in FP^* with minimum length.

```

1: function GROUPEDTSP( $FP^*$ )
2:    $FP_{\theta_i} \leftarrow fp, \forall fp$  where  $fp.\theta = \theta_i$ 
3:    $S \leftarrow \bigcup FP_{\theta_i}$ 
4:   for all  $FP$  in  $FP_{\theta_i}$  do
5:      $FP_{\theta_i} \leftarrow tsp(FP)$ 
6:   end for
7:   for all  $S$  in  $\mathbb{P}(S)$  do
8:     for  $t$  in  $\{-1, 1\}$  do
9:        $S_0 \leftarrow tsp(S, t)$ 
10:    end for
11:   end for
12:    $S^*, t^* \leftarrow \min length(S_0)$ 
13:   return  $\{S^*, T^*\}$ 
14: end function

```

Fig. 6. Grouped traveling salesman problem for waypoint generation.

software *Terragen 4*. The image stitching result is demonstrated quantitatively. Next, we show both the flight and image-stitching results for a real-world case.

A. Simulation Case

1) *Simulated Scene and Flight Planning*: The synthetic scene addressed in this case study was a lake with a peninsula. The land was bare, but had some natural hills and gullies. This scene was problematic that it had irregularly distributed ground features. The hills and gullies were feature rich. The movement and fluctuation of the water surface were considered in the image rendering so that many false tie points would appear as in reality. The scene is shown in Fig. 7, where the red box indicates the target area with dimensions of 286×482 m. The ground feature points estimated with the methods described

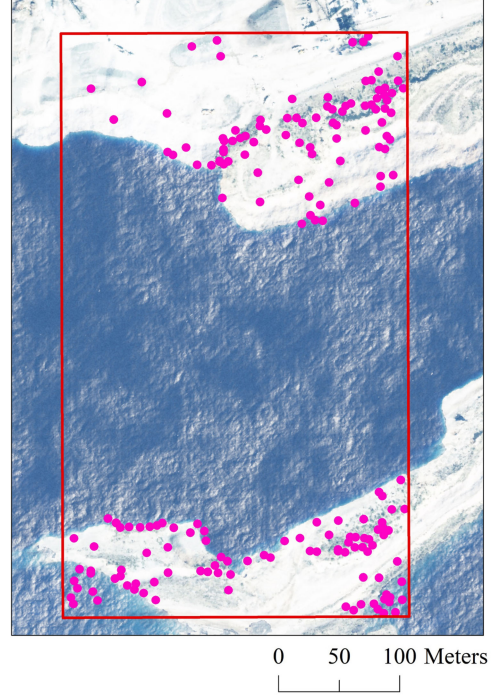


Fig. 7. Synthetic scene and target area. Feature points are marked in pink dots.

in Section II-A1 are indicated with pink dots. The sensor was an APS-C camera with a focal length of 35 mm.

There were three simulated flight paths, two of which were standard paths, and the third was the proposed path. The overlap and sidelap of the two standard paths were 70% and 50%, and 80% and 60%, which are the most common overlaps for UAV photogrammetry. The average overlap of the proposed path was 71.76%, which was calculated by averaging the overlap of adjacent images. The altitude of all paths was set to 200 m. The planning steps of the *proposed path* are shown in the figures in Section II-C2. The lengths of the paths were 3.01, 3.28, and 4.14 km, separately. The number of images for the three paths is

TABLE II
IMAGE STITCHING RESULT AND OVERLAP FOR THE SIMULATION CASE

Flight path	Time for processing	Number of calibrated images/images	Image coverage	3-degree overlap coverage
Standard 2	394s	91/142 (64%)	66.1%	60.3%
Proposed	235s	64/64 (100%)	81.3%	63.1%

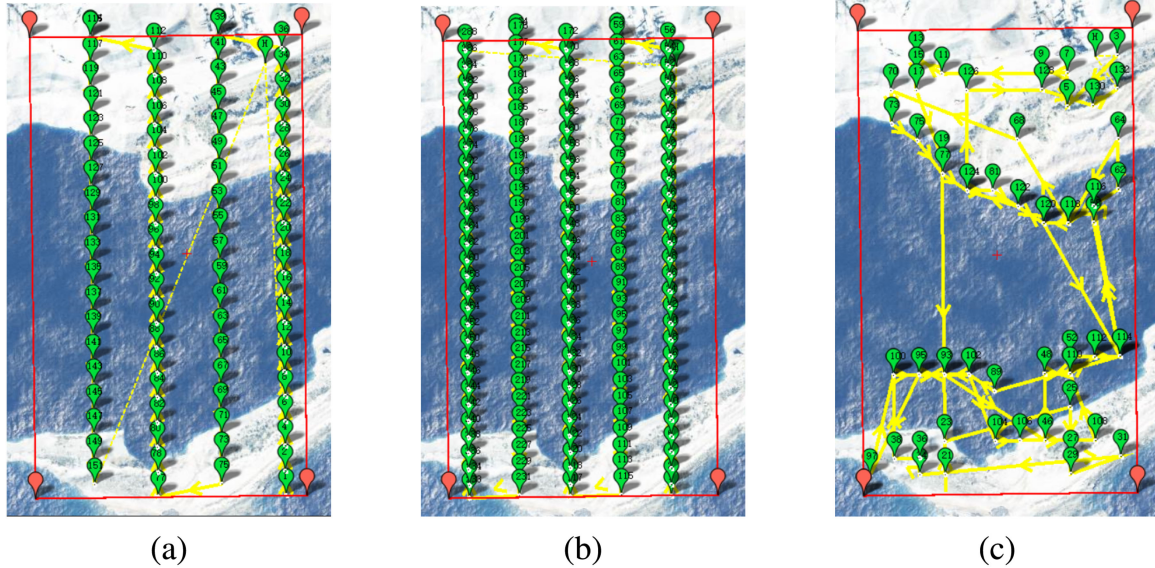


Fig. 8. Flight path for the simulation case. (a) Standard path 1. (b) Standard path 2. (c) Proposed path. Target area is marked with a red rectangle; yellow arrows indicate flight paths and green markers are image shutter locations.

listed in Table II, and that for the *proposed path* was the lowest. An overview of these flight paths is shown in Fig. 8.

2) *Results*: Simulated images were rendered according to the locations and orientations planned in the previous step. Multiple results of image stitching are listed to compare the efficiency of the proposed method with the standard flight paths. The images from the *Standard path 1* were failed to be calibrated by the *Pix4Dmapper*. This may be caused by the large water area that some images contain, which can lead to a significant amount of false tie points. The image stitching and overlap results are listed in Table II. As can be seen in Table II, the *proposed path* required significantly less time for image stitching, since it had fewer images. All images of the *proposed path* were calibrated, whereas there were 51 uncalibrated images for the *Standard path 2*. The mean reprojection errors of the two paths are within 0.2 pixels.

The computed image positions, image overlap illustration, and orthoimages are shown in three columns in Fig. 9. In the left-hand column, the initial positions appear in green, the computed image positions are in blue with uncertainty ellipses, and the uncalibrated images are marked in red. The uncalibrated images in *Standard path 2* appear in the lower half of the target area; there are also some images for which the positions were incorrectly computed. These phenomena led to the loss of orthoimage coverage of the land in the lower half. Combining Fig. 9 and Table II, the orthoimage and 3° overlap coverage for *Standard path 2* were 66.1% and 60.3%, respectively. Meanwhile, the

positions of the images in the *proposed path* were all computed, while the images in the lower part had lower uncertainties. The orthoimage covered the land and part of the surrounding water, which was 15.2% higher than that of *Standard path 2*. The 3° overlap coverage was also 3.2% higher.

B. Real-World Case

1) *Case Study Area and Flight Planning*: The area addressed in the case study was in the vicinity of Meilan Lake in Shanghai, China. The target area, whose dimensions were 553 × 405 m, contained lake water, vegetation, buildings, and roads. The ground features in this area were irregularly distributed. The man-made objects are feature rich, while the vegetation provides fewer feature points. The water may contain many false tie points owing to its movement and reflection. The target area and its surroundings are shown in Fig. 10, where the pink dots represent the estimated ground feature points.

The UAV platform was a DJI Mavic Pro quadrotor. The embedded gimbal camera had a lens with an equivalent focal length of 28 mm. The setup of the flight paths was similar to that in the simulation. There were two standard paths and one proposed path. The overlap and sidelap of the standard paths are the same as the simulated case. The average overlap of the proposed path was 69.44%. The altitude of all paths was set to 100 m. The length of the paths were 3.74, 4.87, and 7.63 km, separately. The number of images for the three paths is listed in Table III.

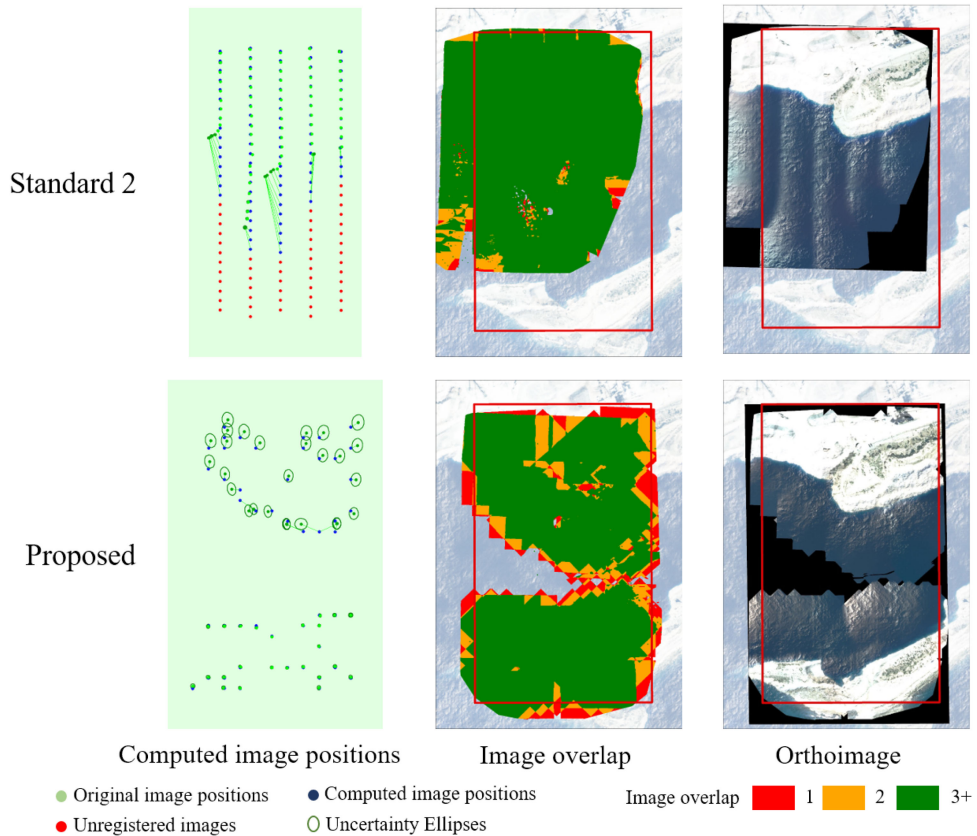


Fig. 9. Image stitching result of the simulation case.

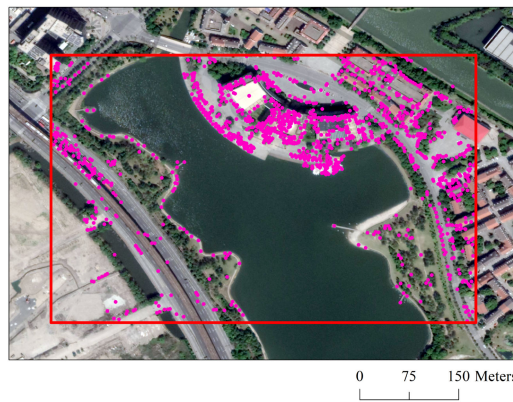


Fig. 10. Target area and feature points of the real-world case.

TABLE III
IMAGE STITCHING RESULT AND OVERLAP FOR THE REAL-WORLD CASE

Flight path	Time for processing	Number of calibrated images/images	Image coverage	3-degree overlap coverage
Standard 1	437s	120/126 (95%)	99.8%	97.7%
Standard 2	934s	239/247 (96%)	100%	99.2%
Proposed	408s	99/100 (99%)	99.8%	95.1%

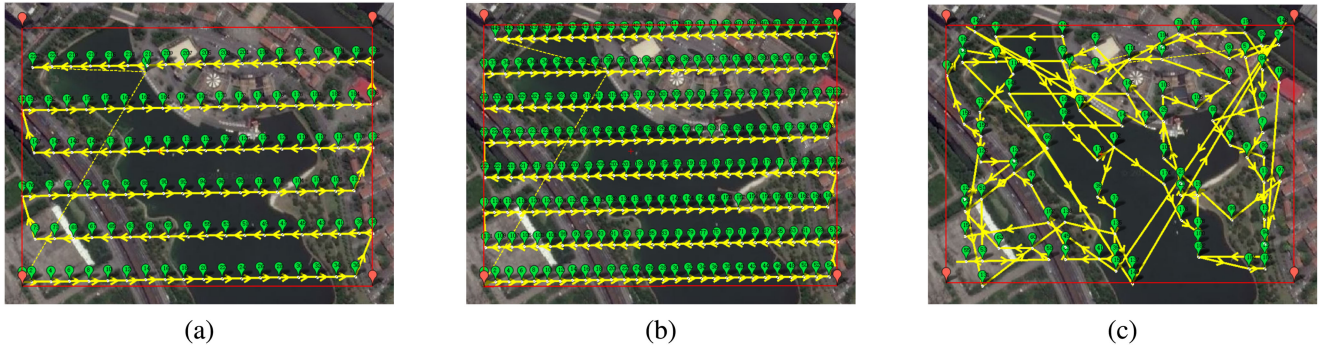


Fig. 11. Flight path for real-world case. (a) Standard path 1. (b) Standard path 2. (c) Proposed path. Target area is marked with red rectangle; yellow arrows indicate flight paths and green markers are image shutter locations.

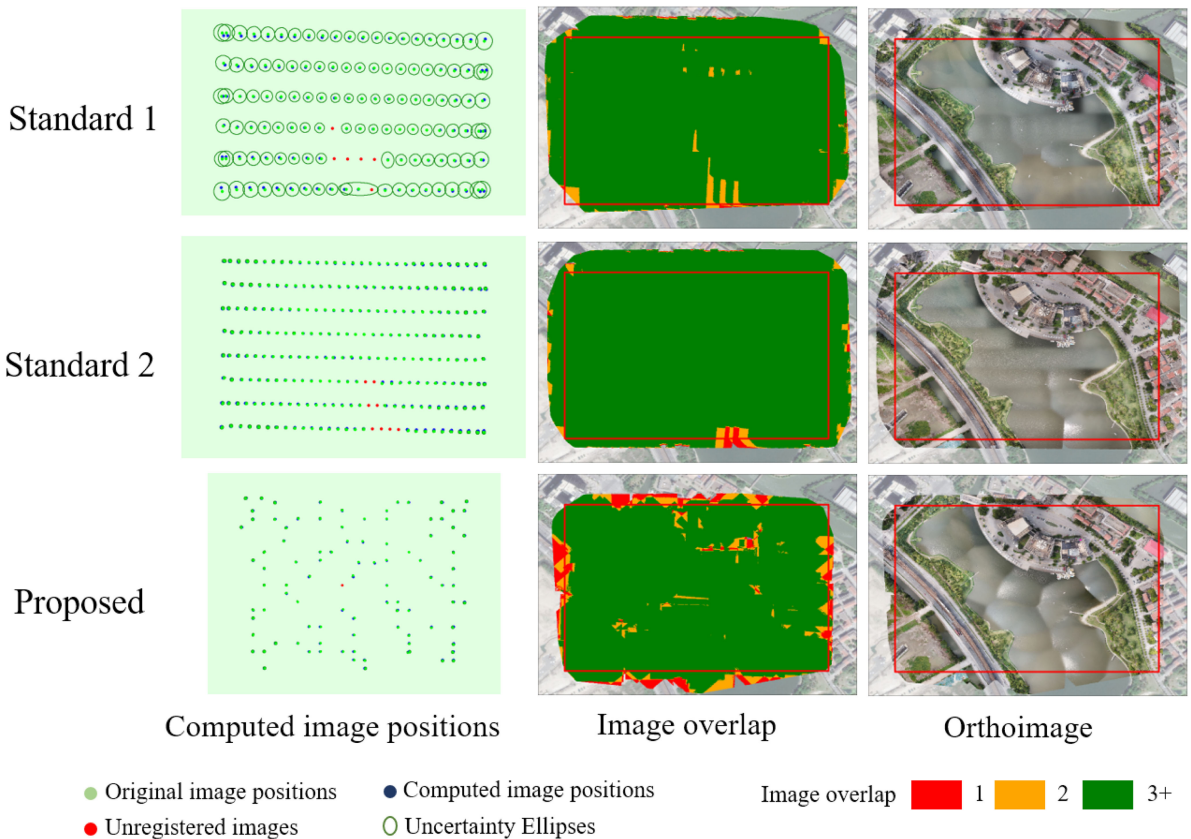


Fig. 12. Image stitching result of the real-world case.

The *proposed path* was the longest, but has the minimum number of images. Three flight paths are shown in Fig. 11.

2) *Results*: The images for each flight path were input to the *Pix4Dmapper*. The image positions provided by the onboard navigation GPS of the UAV were regarded as being the initial positions for AT. The parameters of the camera was fetched from the internal database of the software and were self-calibrated during the process. The statistics for the image-stitching result and overlap are listed in Table III. In this real-world case, orthoimages for all paths were successfully generated, unlike in the simulation case. The *proposed path* had the fewest number of images, and hence, consumed the least processing time. The

standard paths had a similar proportion of calibrated images, while that of the *proposed path* reached 99%. The *proposed path* had the same image coverage with *Standard 1*. However, the 3° overlap coverage was 2.6% less. The *Standard 2* with the higher overlap had the highest image coverage and 3° overlap coverage. The mean reprojection errors of the paths are all within 0.3 pixels,; there is no significant difference in overall accuracy between the *proposed path* and the standard paths.

Fig. 12 shows the computed image positions, image overlap, as well as the orthoimages. As can be seen from the first column, unregistered images for the standard paths were distributed in the lower-middle part of the target area, given that this area is

entirely water. However, images in this area of the *proposed path* were georegistered. The only unregistered image was located in the middle. The image overlap for the standard paths was evenly distributed, except for the lower-middle area. For the *proposed path*, the image overlap was not evenly distributed in the area with buildings, mainly at the edge and in the upper middle of the target area. As seen from the right column, orthoimages of all flight paths covered the majority of the target area. However, the orthoimage of the *proposed path* missed a small part of the upper right, where there is another river. The *proposed path* had a better coverage efficiency since the orthoimages covered less area outside the target surveying area.

IV. CONCLUSION AND FUTURE WORK

We proposed a novel path-planning method for UAV-based mapping in problematic areas. This method is ground feature oriented, whereby feature points are estimated from a low-resolution image, after which image footprints are generated using three-step optimization. This approach ensures the georegistration of images during orthoimage stitching while maximizing the orthoimage coverage. A modified SIFT detector and an SVM filter together estimate the potential tie points for image stitching from a low-resolution image. The three-step submodular optimization first selects images to cover all feature points, then maximizes the image coverage, and finally, adds images that ensure image overlap and georegistration.

Two cases, a simulation and a real-world case, were selected to evaluate the proposed ground feature oriented path-planning method, both qualitatively and quantitatively, in terms of image registration and coverage. The proposed method was compared with the standard “lawnmower” path-planning methods with different overlaps. The results showed that the proposed method covered the same area with the fewest number of images. The comprehensive orthoimage coverage of the proposed method was similar to that attained with the standard paths, while the coverage of the “feature poor” area was significantly better. With the proposed method, more images for which the shutter positions were above the water were successfully georegistered. Therefore, for areas with irregularly distributed ground features, the proposed method can obtain a more complete orthoimage coverage than the standard methods. However, we cannot assure that the data processing will fully exclude the possibility of false positives, incorrect rotation, or distortion.

The novelty of the proposed method is that it provides a path-planning solution that is capable of obtaining orthoimages for problematic areas with coverage that is as complete as possible. The present method ensures the georegistration and 3° overlap coverage with fewer images, which may improve the efficiency of the post processing. Unlike traditional path-planning methods, such as [31] and [32], the present study took the distribution of ground features into consideration. Compared to the DG methods described in [10] and [11], the proposed method requires no precise overall system calibration. Moreover, the path-planning solution is much cheaper and can be executed by more surveying or consumer UAV platforms. Compared to similar information-driven path-planning methods [48], [49], the

present study had a different objective, and thus, the information was defined differently.

The present study was based on a hypothesis that the target area is flat. However, in reality, the presence of buildings and terrain fluctuation affects the image overlap. Therefore, this ideal hypothesis may result in incomplete image coverage, as shown in the middle column of Fig. 12. Our future work will consider the impact of the terrain on image coverage. Second, the planning of the images relies on estimating the ground feature points. So far, we have only provided a quick and simple approach to support path planning. Therefore, a better and more robust ground feature estimation method should also be developed in the future. On the contrary, longer and more complex paths were used in the proposed study; sharp turns also made the execution of the path less stable. This is because of the lack of path optimization. In future, we plan to apply more constraints to the waypoint generation and further introduce collaborative path planning, thus increasing the stability and efficiency of UAV execution. Another alternative and relevant application of the proposed method is post processing. The same method can be applied with a densely captured dataset to select optimal images to acquire a more efficient processing dataset.

ACKNOWLEDGMENT

The authors would like to thank Shanghai Tongfan Surveying Engineering and Technology Co., Ltd., for their technical support regarding the UAVs.

REFERENCES

- [1] A. C. Watts, V. G. Ambrosia, and E. A. Hinkley, “Unmanned aircraft systems in remote sensing and scientific research: Classification and considerations of use,” *Remote Sens.*, vol. 4, no. 6, pp. 1671–1692, 2012.
- [2] L. Matikainen *et al.*, “Remote sensing methods for power line corridor surveys,” *ISPRS J. Photogrammetry Remote Sens.*, vol. 119, pp. 10–31, 2016.
- [3] T. T. Sankey, J. McVay, T. L. Swetnam, M. P. McClaran, P. Heilman, and M. Nichols, “UAV hyperspectral and lidar data and their fusion for arid and semi-arid land vegetation monitoring,” *Remote Sens. Ecology Conserv.*, vol. 4, pp. 20–33, 2017.
- [4] L. Wallace, A. Lucieer, C. Watson, and D. Turner, “Development of a UAV-lidar system with application to forest inventory,” *Remote Sens.*, vol. 4, no. 6, pp. 1519–1543, 2012.
- [5] Y. Vacanas, K. Themistocleous, A. Agapiou, and D. Hadjimitsis, “Building information modelling (BIM) and unmanned aerial vehicle (UAV) technologies in infrastructure construction project management and delay and disruption analysis,” in *Proc. Int. Conf. Remote Sens. Geoinformation Environ.*, 2015, pp. 95350C–95350C-11.
- [6] K. Themistocleous, M. Ioannides, A. Agapiou, and D. G. Hadjimitsis, “The methodology of documenting cultural heritage sites using photogrammetry, UAV, and 3D printing techniques: The case study of Asinou church in Cyprus,” in *Proc. 3rd Int. Conf. Remote Sens. Geoinformation Environ.*, vol. 9535, 2015, p. 953510.
- [7] U. Niethammer, M. James, S. Rothmund, J. Travelletti, and M. Joswig, “UAV-based remote sensing of the super-sauze landslide: Evaluation and results,” *Eng. Geol.*, vol. 128, pp. 2–11, 2012.
- [8] H. Eisenbeiß, “UAV photogrammetry,” Ph.D. dissertation, Dept. Civil, Environmental Geomatic Eng., Inst. Geodesy and Photogrammetry, ETH Zurich, Zurich, Switzerland, 2009.
- [9] N. Micheletti, J. H. Chandler, and S. N. Lane, “Structure from motion (SfM) photogrammetry,” in *Geomorphological Techniques*. London, U.K.: British Society for Geomorphology, 2015.
- [10] M. M. Mostafa and J. Hutton, “Direct positioning and orientation systems: How do they work? What is the attainable accuracy,” in *Proc. Amer. Soc. Photogrammetry Remote Sens. Annu. Meeting, St. Louis, MO, USA*, 2001, pp. 23–27.

- [11] P. E. Carbonneau and J. T. Dietrich, "Cost-effective non-metric photogrammetry from consumer-grade suas: Implications for direct georeferencing of structure from motion photogrammetry," *Earth Surface Processes Landforms*, vol. 42, no. 3, pp. 473–486, 2017.
- [12] M. Cramer, D. Stallmann, and N. Haala, "Direct georeferencing using GPS/inertial exterior orientations for photogrammetric applications," *Int. Arch. Photogrammetry Remote Sens.*, vol. 33, pp. 198–205, 2000.
- [13] P. Gabrlik, A. I. Cour-Harbo, P. Kalvodova, L. Zalud, and P. Janata, "Calibration and accuracy assessment in a direct georeferencing system for UAS photogrammetry," *Int. J. Remote Sens.*, vol. 39, pp. 1–29, 2018.
- [14] M. Cramer, "Direct geocoding—Is aerial triangulation obsolete?" in *Photogrammetric Week '99*, D. Fritsch and R. Spiller, Eds., Heidelberg, Germany: Wichmann Verlag, 1999, pp. 59–70.
- [15] D. G. Lowe, "Distinctive image features from scale-invariant keypoints," *Int. J. Comput. Vision*, vol. 60, no. 2, pp. 91–110, 2004.
- [16] M. A. Fischler and R. C. Bolles, "Random sample consensus: A paradigm for model fitting with applications to image analysis and automated cartography," in *Commun. ACM*. Elsevier, vol. 24, no. 6, pp. 381–395, Jun. 1981.
- [17] D. Gonzalez Aguilera *et al.*, "Graphos opensource software for photogrammetric applications," *Photogrammetric Rec.*, vol. 33, no. 161, pp. 11–29. [Online]. Available: <https://onlinelibrary.wiley.com/doi/abs/10.1111/phor.12231>
- [18] J. L. Schönberger and J.-M. Frahm, "Structure-from-motion revisited," in *Proc. Conf. Comput. Vision Pattern Recognit.*, 2016.
- [19] M. Pierrot-Deseilligny, Micmac. (2018). [Online]. Available: <https://micmac.ensg.eu/index.php/Accueil>
- [20] C. Wu *et al.*, *Visualsfm: A Visual Structure From Motion System*. (2011). [Online] Available: <http://ccwu.me/vsfm/>
- [21] K. Mikolajczyk and C. Schmid, "A performance evaluation of local descriptors," *IEEE Trans. Pattern Anal. Mach. Intell.*, vol. 27, no. 10, pp. 1615–1630, Oct. 2005.
- [22] Y. Ke and R. Sukthankar, "PCA-sift: A more distinctive representation for local image descriptors," in *Proc. IEEE Comput. Soc. Conf. Comput. Vision Pattern Recognit.*, vol. 2, pp. 506–513, 2004.
- [23] Z. Wang, F. Wu, and Z. Hu, "MSLD: A robust descriptor for line matching," *Pattern Recognit.*, vol. 42, no. 5, pp. 941–953, 2009.
- [24] H. Kim and S. Lee, "A novel line matching method based on intersection context," in *Proc. IEEE Int. Conf. Robot. Autom.*, 2010, pp. 1014–1021.
- [25] Y. Sun, L. Zhao, S. Huang, L. Yan, and G. Dissanayake, "Line matching based on planar homography for stereo aerial images," *ISPRS J. Photogrammetry Remote Sens.*, vol. 104, pp. 1–17, 2015.
- [26] M. Cho, J. Sun, O. Duchenne, and J. Ponce, "Finding matches in a haystack: A max-pooling strategy for graph matching in the presence of outliers," in *Proc. IEEE Conf. Comput. Vision Pattern Recognit.*, 2014, pp. 2083–2090.
- [27] X. Yuan, S. Chen, W. Yuan, and Y. Cai, "Poor textural image tie point matching via graph theory," *ISPRS J. Photogrammetry Remote Sens.*, vol. 129, pp. 21–31, 2017. [Online]. Available: <http://www.sciencedirect.com/science/article/pii/S0924271617302423>
- [28] M. May, M. J. Turner, and T. Morris, "Scale invariant feature transform: A graphical parameter analysis," in *Proc. British Mach. Vision Conf. U.K. Postgraduate Workshop*, 2010, pp. 5–1.
- [29] A. A. Sima and S. J. Buckley, "Optimizing SIFT for matching of short wave infrared and visible wavelength images," *Remote Sens.*, vol. 5, no. 5, pp. 2037–2056, 2013.
- [30] S. Castillo-Carrión and J.-E. Guerrero-Ginel, "SIFT optimization and automation for matching images from multiple temporal sources," *Int. J. Appl. Earth Observ. Geoinformation*, vol. 57, pp. 113–122, 2017.
- [31] A. Xu, C. Viriyasuthee, and I. Rekleitis, "Optimal complete terrain coverage using an unmanned aerial vehicle," in *Proc. IEEE Int. Conf. Robot. Autom.*, 2011, pp. 2513–2519.
- [32] M. M. Trujillo, M. Darrah, K. Speransky, B. DeRoos, and M. Wathen, "Optimized flight path for 3d mapping of an area with structures using a multirotor," in *Proc. Int. Conf. Unmanned Aircr. Syst.*, 2016, pp. 905–910.
- [33] E. Galceran and M. Carreras, "A survey on coverage path planning for robotics," *Robot. Auton. Syst.*, vol. 61, no. 12, pp. 1258–1276, 2013.
- [34] W. H. Huang, "Optimal line-sweep-based decompositions for coverage algorithms," in *Proc. IEEE Int. Conf. Robot. Autom.*, vol. 1, 2001, pp. 27–32.
- [35] Y. Li, H. Chen, M. J. Er, and X. Wang, "Coverage path planning for UAVs based on enhanced exact cellular decomposition method," *Mechatronics*, vol. 21, no. 5, pp. 876–885, 2011.
- [36] J. I. V. Gomez, M. M. Melchor, and J. C. H. Lozada, "Optimal coverage path planning based on the rotating calipers algorithm," in *Proc. Int. Conf. Mechatronics, Electron. Automot. Eng.*, 2017, pp. 140–144.
- [37] G. S. Avellar, G. A. Pereira, L. C. Pimenta, and P. Iscold, "Multi-UAV routing for area coverage and remote sensing with minimum time," *Sensors*, vol. 15, no. 11, pp. 27 783–27 803, 2015.
- [38] H. Seyyedhasani and J. S. Dvorak, "Using the vehicle routing problem to reduce field completion times with multiple machines," *Comput. Electron. Agriculture*, vol. 134, pp. 142–150, 2017.
- [39] C. Di Franco and G. Buttazzo, "Energy-aware coverage path planning of UAVs," in *Proc. IEEE Int. Conf. Auton. Robot Syst. Competitions*, 2015, pp. 111–117.
- [40] C. Di Franco and G. Buttazzo, "Coverage path planning for UAVs photogrammetry with energy and resolution constraints," *J. Intell. Robot. Syst.*, vol. 83, no. 3–4, pp. 445–462, 2016.
- [41] R. A. Martin, I. Rojas, K. Franke, and J. D. Hedengren, "Evolutionary view planning for optimized UAV terrain modeling in a simulated environment," *Remote Sens.*, vol. 8, no. 1, p. 26, 2015.
- [42] W. R. Scott, G. Roth, and J.-F. Rivest, "View planning for automated three-dimensional object reconstruction and inspection," *ACM Comput. Surv.*, vol. 35, no. 1, pp. 64–96, 2003.
- [43] W. Jing and K. Shimada, "Model-based view planning for building inspection and surveillance using voxel dilation, medial objects, and random-key genetic algorithm," *J. Comput. Des. Eng.*, vol. 5, pp. 337–347, 2017.
- [44] B. Alsadik, M. Gerke, and G. Vosselman, "Automated camera network design for 3d modeling of cultural heritage objects," *J. Cultural Heritage*, vol. 14, no. 6, pp. 515–526, 2013.
- [45] A. H. Ahmadabadian, S. Robson, J. Boehm, and M. Shortis, "Stereoscopy network design for precise and dense 3d reconstruction," *Photogrammetric Rec.*, vol. 29, no. 147, pp. 317–336, 2014.
- [46] M. Popovi, G. Hitz, J. Nieto, I. Sa, R. Siegwart, and E. Galceran, "Online informative path planning for active classification using UAVs," in *Proc. IEEE Int. Conf. Robot. Autom.*, Singapore, May 2017, pp. 5753–5758.
- [47] E. Palazzolo and C. Stachniss, "Effective exploration for MAVs based on the expected information gain," *Drones*, vol. 2, no. 1, p. 9, 2018.
- [48] B. Hepp, M. Nießner, and O. Hilliges, "Plan3d: Viewpoint and trajectory optimization for aerial multi-view stereo reconstruction," 2017, arXiv: 1705.09314.
- [49] M. Roberts *et al.*, "Submodular trajectory optimization for aerial 3d scanning," 2017, arXiv: 1705.00703.
- [50] A. Krause and D. Golovin, "Submodular function maximization," in *Tractability: Practical Approaches to Hard Problems*. Cambridge, U.K.: Cambridge Univ. Press, 2014.
- [51] T. Lindeberg, *Scale-Space Representation: Definition and Basic Ideas*. (1997). [Online]. Available: <http://www.csc.kth.se/~tony/cern-review/cern-html/node2.html>
- [52] N. Cristianini and J. Shawe-Taylor, *An Introduction to Support Vector Machines and other Kernel-based Learning Methods*. Cambridge, U.K.: Cambridge Univ. Press, 2000.



Chun Liu received the B.E. and M.E. degrees in surveying and mapping from Shandong University of Science and Technology, Tai'an, Shandong, China, in 1995 and 1998, respectively, and the Ph.D. degree in geodesy and surveying from Tongji University, Shanghai, China, in 2001.

From 2001 to 2003, he was a Visiting Scholar with Development of Infrastructure for Cyber Hong Kong, The Hong Kong Polytechnic University, China. From 2007 to 2008, he was a Senior Visiting Scholar with the Laboratory of Mapping and GIS, Ohio State University, Columbus, OH, USA. In 2011, he was a Senior Visiting Scholar with Institute of Spatial Geodesy and Engineering Survey, the University of Nottingham, Nottingham, U.K. He is currently a Full Professor of Cartography and Geography Information Engineering with the College of Surveying and Geomatics, Tongji University, Shanghai. His research interests include indoor mapping, the theory and application of surveying UAV, sensor fusion, LiDAR data interpretation, and manifold learning of hyperspectral imagery.



Shuhang Zhang received the B.E. degree in geography information system from Tongji University, Shanghai, China, in 2014. He is currently working toward the Ph.D. degree with the College of Surveying and Geo-informatics, Tongji University, Shanghai.

His research interests include UAV-based remote sensing and photogrammetry data acquisition, coverage path planning for UAV mapping, and UAV cooperative mapping.



Akram Akbar received the B.E. degree in aircraft manufacturing engineering from Tongji University, Shanghai, China, in 2016. He is currently working toward the Ph.D. degree with the College of Surveying and Geo-informatics, Tongji University, Shanghai.

His research interests include UAV-based surveying and mapping, especially on intelligent control and planning of surveying and mapping UAV, multisensor integration, and data analysis.